

# Experimental characterization of anode heating by electron emission from a multi-walled carbon nanotube

T. Westover<sup>a</sup>, T.S. Fisher<sup>a,\*</sup>, F. Pfefferkorn<sup>b</sup>

<sup>a</sup> School of Mechanical Engineering, and Birck Nanotechnology Center, Purdue University, West Lafayette, IN 47907, USA

<sup>b</sup> Department of Mechanical Engineering, University of Wisconsin-Madison, Madison, WI 53706, USA

Received 18 January 2006; received in revised form 15 July 2006

Available online 2 October 2006

## Abstract

The steady-state temperature distribution in a thin anode bombarded by an electron beam field emitted from an individual multi-walled carbon nanotube is measured with an infrared camera, and this distribution is compared to that predicted by a numerical model. By assuming the electron distribution in the beam follows a Gaussian distribution, a good fit to the anode temperature profile is obtained and this fit provides an estimate of the beam spreading radius. Results indicate the electron beam narrows as the emission current increases. A heat flux on the anode surface as high as  $0.35 \text{ W/cm}^2$  has been measured, corresponding to an electron beam radius of approximately 1.22 mm.

© 2006 Elsevier Ltd. All rights reserved.

**Keywords:** Field emission; Carbon nanotube; Anode heating

## 1. Introduction

Efficient electron field emitters are becoming increasingly attractive for a wide range of applications, including scanning probe tips, power electronics, and flat panel displays [1,2]. Advances in microfabrication techniques now promise to extend the range of devices employing field emission by utilizing emitters arranged in patterned arrays. Cathodes consisting of materials such as carbon nanotubes and polycrystalline diamond have demonstrated high rates of field emission at relatively low applied electric fields, although the emission generally occurs at nanoscale sites on the cathode where the local electric field is greatly enhanced [3,4]. Emitted electrons accelerate under the applied electric field as they traverse a vacuum gap and ultimately impact the anode. This energetic electron beam can produce substantial heating in a localized region within the anode, causing thermal stresses and possibly failure [5].

Fisher et al. [6] used a Monte Carlo technique to determine the spatial distribution of the electrons in a beam originating from a point source cathode, and from this simulation estimated heat generation occurring within an anode due to the penetration of the electron beam beneath the anode surface. In a series of field emission experiments, Harris et al. [7] employed a polycrystalline diamond film as an electron source to bombard a steel anode. By measuring the anode temperature rise, they were able to estimate the total rate of energy absorbed by the anode and the approximate area over which the heating was confined. The present study utilizes an individual multi-walled carbon nanotube (MWNT) as the electron source in order to evaluate the heating caused by electron emission from a single nanoscale emission site.

Fowler and Nordheim [8] first described the physics governing field emission from a flat surface. Since that time, elongated emitter structures have been shown to enhance the local electric field greatly and thus enable emission under reduced applied electric fields [9]. With turn-on fields measured below  $5 \text{ V}/\mu\text{m}$ , carbon nanotubes are extremely

\* Corresponding author. Tel.: +1 765 494 5627; fax: +1 765 494 0539.  
E-mail address: [tsfisher@purdue.edu](mailto:tsfisher@purdue.edu) (T.S. Fisher).

## Nomenclature

$b$	slope of infrared camera calibration curve	$u_{\sigma}$	total uncertainty in the electron beam radius
$I$	mean measured electrical current	$u_{\sigma\text{fit}}$	uncertainty in the electron beam radius due to least-squares fit
$k_{\text{eff}}$	effective thermal conductivity of anode	$u_{\sigma T}$	uncertainty in the electron beam radius due to temperature measurement uncertainty
$k_p$	thermal conductivity of paint	$u_{\sigma Q}$	uncertainty in the electron beam radius due to heating uncertainty
$k_s$	thermal conductivity of stainless steel	$u_{\sigma\Delta z}$	uncertainty in the electron beam radius due to anode thickness uncertainty
$N$	number of data points used in the least-squares fit	$V$	applied voltage potential
$q''$	local heat flux	<i>Greek symbols</i>	
$q''_{\text{max}}$	maximum heat flux	$\Delta z_p$	width of paint layer on anode surface
$Q$	energy deposition rate on the anode surface	$\Delta z_s$	width of stainless steel in anode
$r$	anode radial coordinate	$\theta_{Q,r=0}$	local sensitivity coefficient at $r=0$ correlating predicted temperature rise to total anode heating
$R$	anode radius	$\theta_{\Delta z,r=0}$	local sensitivity coefficient at $r=0$ correlating predicted temperature rise to anode thickness
$S$	estimate of the variability of the data taken by the infrared camera	$\theta_{\sigma,i}$	local sensitivity coefficient at data point $i$ correlating predicted temperature rise to electron beam radius
$t_{95,N-1}$	$t$ estimator with 95% probability and $N-1$ degrees of freedom	$\phi_Q$	sensitivity coefficient correlating predicted maximum heat flux to total anode heating
$T_{\text{data},i}$	mean measured anode temperature rise at location $r_i$	$\phi_{\sigma}$	sensitivity coefficient correlating predicted maximum heat flux to electron beam radius
$T_{\text{pred},i}$	predicted temperature at location $r_i$	$\sigma_e$	beam radius, a parameter characterizing the spread of the electron beam
$u_b$	uncertainty in slope of infrared camera calibration curve		
$u_{\text{CAM}}$	least-count uncertainty of infrared camera		
$u_{q_{\text{max}}}$	uncertainty in maximum heat flux on anode surface		
$u_Q$	uncertainty in total anode heating		
$u_T$	total uncertainty in temperature measurement with infrared camera		
$u_{\Delta z}$	uncertainty in the anode thickness		

efficient emitters [10]. Recent experiments report that carbon nanotubes may support local current densities as high as  $10^9$  A/cm<sup>2</sup> [11,12], and that emitter arrays may be able to produce substrate-level current densities as high as  $10^5$  A/cm<sup>2</sup> [12].

Experiments reveal that single-walled nanotubes and open-ended multi-walled nanotubes can produce ring-like current density patterns, indicating that emission occurs primarily from the nanotube ends [13,14]. Mayer et al. [15–17] employed an atomistic transfer matrix method to simulate emission from various types of carbon nanotubes by assuming a constant electric field in the vicinity of the electric tip. More recently, Walker et al. [18] performed similar simulations including Coulomb interactions among the electrons, non-axial field components at the nanotube tip, and random non-axial momentum components of the electrons at emission, and confirmed the possibility that ring-type patterns can occur in the electron beam.

The present work provides an experimental extension of theoretical anode heating studies. In the following sections, the experimental setup is first described, and then the electron beam and anode heating models are introduced. Experimental data are then presented and analyzed to estimate of the electron beam radius and the maximum heat

flux on the anode surface for different applied electric fields and emission currents.

## 2. Experimental setup

Fig. 1 contains a schematic of the experimental apparatus used to measure the heating effect at the anode produced by field emitted electrons. The anode (a stainless steel disc having a diameter of 36.7 mm and thickness of 0.025 mm) was fixed between a vertical plate and a metal ring. A hole in the vertical plate with a diameter of 18.9 mm ensured that the central portion of the anode's rear face was exposed to enable temperature measurements with an infrared camera placed outside the vacuum chamber. The cathode consisted of an individual MWNT mounted on a tungsten tip that was fastened to the end of a metal rod. A groove in the cathode platform served to align the tungsten tip along the anode axis. The vertical plate and the cathode platform were electrically isolated from the base by means of ceramic spacers, ensuring that both the anode and cathode were electrically isolated from the other components in the vacuum chamber.

The tungsten tip was etched using the DC drop-off method commonly employed in scanning electron micro-

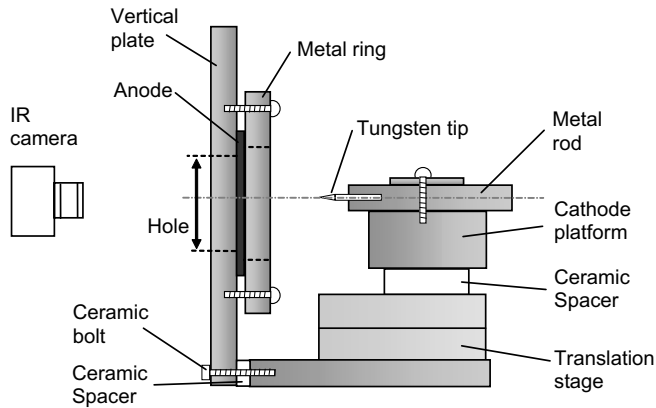


Fig. 1. Schematic of the experimental apparatus.

scopy (SEM) applications [19]. In this process, a tungsten wire of diameter 0.25 mm is dipped approximately 5 mm into a 2 N NaOH solution. A voltage potential of 10 VDC is then applied to the tungsten wire while maintaining a graphite rod in the solution at zero potential. The resulting electrochemical reaction etches the tungsten wire at the surface of the NaOH solution, causing the tip of the wire to detach from the body and leaving a sharp point on the end of the tungsten wire.

Mounting of the nanotube to the etched tungsten tip was performed using two micromanipulators (Newport M-460A-XYZ) aided by an inverted optical microscope (Nikon Epiphot 200) equipped with a 50 $\times$ /0.55 objective to observe the process in darkfield at 750 $\times$  magnification. A mesh of MWNTs was placed on a section of SEM tape, with individual nanotubes protruding from the edges of the mesh. The MWNT mesh was synthesized using a previously reported technique [20]. Before mounting a MWNT on the tungsten tip, a small amount of electrically conductive adhesive was placed on the tip by carefully touching it to a clean portion of carbon tape (Ted Pella, Inc.) and removing it. The tungsten tip with adhesive from the tape was then moved to one of the protruding nanotubes and positioned such that the nanotube became attached to the tip. A MWNT attached to the etched tungsten tip in this way withstood the applied electric fields encountered during field emission.

Fig. 2 shows a MWNT mounted on an etched tungsten tip at 750 $\times$  magnification. Subsequently, the anode was held stationary, and the etched tungsten tip was fixed to a linear translation stage so that the vacuum gap distance could be adjusted. This arrangement was necessary so that the vacuum gap distance could be determined after each experiment by carefully stepping the anode platform in measured increments until contact was made with the cathode. The entire experimental apparatus was placed within a vacuum chamber that was maintained at a pressure of approximately  $5 \times 10^{-7}$  Torr during experiments.

The temperature profile of the anode was measured by a ThermoCAM SC300 infrared camera placed outside the vacuum chamber. A germanium viewport in the vacuum

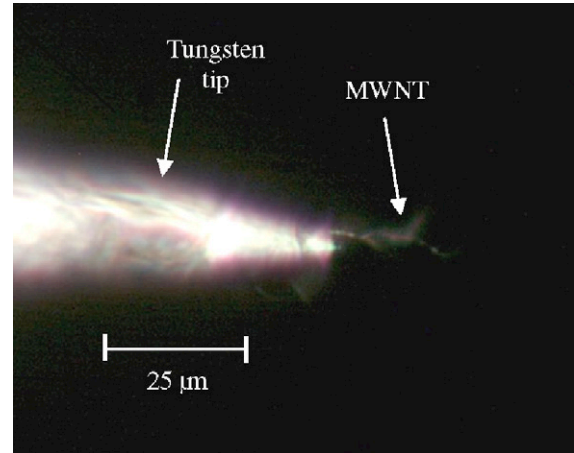


Fig. 2. An individual multi-walled carbon nanotube mounted on an etched tungsten tip. Magnification is 750 $\times$ .

chamber wall allowed the infrared camera to view the back surface of the anode, which was coated with flat black paint to achieve a surface emissivity of approximately 0.94. Experiments have demonstrated that the germanium viewport in the vacuum chamber wall affects infrared camera measurements and increases the measurement uncertainty. Consequently, calibration experiments were conducted to account for the effect of viewing objects in vacuum through this viewport.

The calibration scale shown in Fig. 3 was generated by viewing a painted aluminum bar at a vacuum pressure of approximately  $10^{-6}$  Torr. The temperature of the aluminum bar was increased using an internal heater and was allowed to reach steady-state before measuring the surface temperature at two locations with thermocouples. Calibration of the infrared camera consists of determining the ratio of the actual temperature change measured by the thermocouples to the temperature change registered by the IR camera, which corresponds to the slope,  $b$ , of the curve in Fig. 3. For the experiments in this study, the slope of the calibration curve is 2.55, and multiple experiments demonstrated that this relationship was consistent during

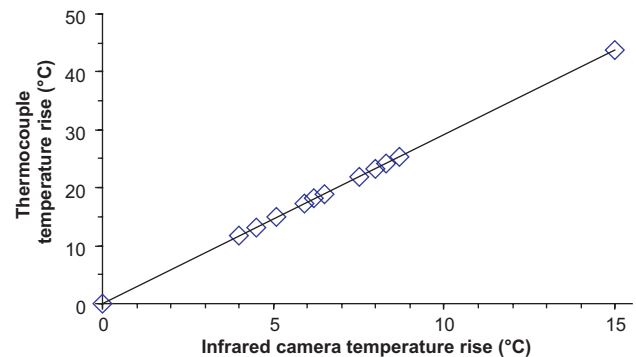


Fig. 3. Temperature rise measurements taken in vacuum with thermocouples and an infrared camera viewing through a germanium viewport. The specimen was an aluminum bar painted flat black.

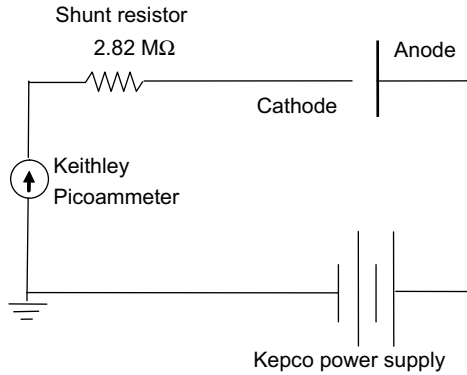


Fig. 4. Schematic diagram of the electrical circuit for measuring current-voltage field emission characteristics.

the period in which the experiments were performed. The uncertainty in the slope of the calibration curve,  $u_b$ , may be determined following the procedure outlined by Bowker for estimating the slope of a line when the offset is known to be zero [21]. Using this procedure, a value of 0.024 is found for  $u_b$ .

The uncertainty,  $u_T$ , associated with a temperature measurement using the infrared camera can then be estimated as

$$u_T = \sqrt{(u_{CAM})^2 + \left(\frac{u_b}{b} T\right)^2 + (U_{TC} T)^2} \quad (1)$$

where  $T$  is the actual temperature rise and  $u_{CAM}$  is the least-count uncertainty of the infrared camera viewing through a germanium viewport, approximately equal to 0.4 °C.  $U_{TC}$  is the percent uncertainty in the thermocouple temperature rise measurement, which was estimated as  $\pm 2\%$ . This simple calibration is sufficient for the present work because the anode heating experiments depend principally on measured values of temperature changes, which are related solely to the slope of the calibration line.

A schematic diagram of the experimental circuit appears in Fig. 4. A Kepco BKH1000-0.2 MG power supply provided the electric potential bias to induce field emission, and a Keithley 6486 picoammeter measured the field emission current between the cathode and the anode. The uncertainties in the applied voltage and electric current measurements are each less than 0.5%. Electric current measurements were recorded through an IEEE-488 (GPIB) bus connected to a PCI-GPIB controller. A 2.82 MΩ shunt resistor was included in the circuit to stabilize the field emission current, and coaxial cables were used to connect the instrumentation to reduce EMI and RFI signals.

### 3. Electron beam and anode heating models

Data recorded during field emission experiments included the temperature field of the anode as a function of three parameters: applied voltage, electric current, and vacuum gap distance separating the anode from the cath-

ode. Because temperature variations through the thickness of the anode were negligible, a 1D finite-difference model of the anode was developed to predict the anode temperature field based on experimental conditions, and this temperature field was compared to that obtained from infrared measurements in order to characterize the heating of the anode by the electron beam. The governing equation for the anode temperature,  $T$ , as a function of radial location,  $r$ , may be written as

$$Z \frac{d}{dr} \left( k_{\text{eff}} \cdot r \frac{dT}{dr} \right) - 2 \cdot r \cdot \sigma \cdot \varepsilon (T^4 - T_{\text{surr}}^4) + r \cdot q'' = 0 \quad (2)$$

where  $Z$  and  $k_{\text{eff}}$  represent anode thickness and effective thermal conductivity, respectively.  $\sigma$  is the Stefan–Boltzmann constant ( $5.67 \times 10^{-8} \text{ W/m}^2 \text{ K}^4$ ) and  $q''$  is the local heat flux on the anode surface produced by the electron beam.  $\varepsilon$  is the average anode emissivity, which was calculated by taking the arithmetic mean of the emissivities of both sides of the anode. Assuming an emissivity of 0.94 for the painted side of the anode and an emissivity of 0.16 for the unpainted side,  $\varepsilon$  was estimated to be 0.55. During experiments, the temperature at the outer edge of the anode was observed to increase above that of the metal ring because of thermal contact resistance. Consequently, a Dirichlet boundary condition was imposed at the outer edge of the finite-difference model, holding the temperature at the edge of the anode equal to that measured by the infrared camera. The inner boundary condition was imposed by fixing the first derivative of the temperature with respect to  $r$  equal to zero at the center of the anode, which is equivalent to a Neumann zero flux boundary condition.

Preliminary simulations modeled the heating of the anode surface as a uniform heat flux over a small circle centered on the anode axis. However, those simulations yielded poor fits to the measured data, and their results are not shown. A superior fit to the experimental data was obtained by assuming that the electron beam (and consequently the heating occurring at the anode) followed an axially symmetric Gaussian distribution. The spread of the electron beam was characterized by the standard deviation of the Gaussian distribution, symbolized by  $\sigma_e$  and hereafter called the electron beam radius. The standard deviation,  $\sigma_e$ , was determined by minimizing the sum of the squared errors between the data obtained from the infrared camera and the finite-difference model. With the above assumptions and the constraint that the total heating due to the electron beam must equal the product of the applied voltage,  $V$ , and the measured current,  $I$ , the local heat flux incident on the anode surface takes the form

$$q''(r) = \frac{VI}{2\pi\sigma_e^2(1 - e^{-R^2/2\sigma_e^2})} e^{-r^2/2\sigma_e^2} \quad (3)$$

where  $R$  is the outer radius of the anode.

The paint layer on the anode's back surface was found to have a significant effect on the anode temperature

profile, and, therefore, it was included in the finite-difference model. An effective thermal conductivity of the steel/paint anode was calculated using [22]

$$k_{\text{eff}} = \frac{k_s \Delta z_s + k_p \Delta z_p}{\Delta z_s + \Delta z_p} \quad (4)$$

where  $k_s$  and  $k_p$  are the thermal conductivities of stainless steel and paint with values of 16.3 and 0.65 W/m K, respectively.  $\Delta z_s$  and  $\Delta z_p$  correspond to the thicknesses of the steel and paint layers, with mean measured values of 0.025 and 0.031 mm, respectively. From these values, the effective thermal conductivity of the anode was calculated to be 7.76 W/m K. The accuracy of this effective conductivity model was validated by comparison to a two-dimensional finite-difference model that included the distinct steel and paint layers. However, because the one-dimensional model is computationally more efficient, it was employed in the parameter estimation process to determine the beam radius,  $\sigma_e$ . Comparisons between these models and the dependence of the model results on the mesh size are discussed in the following section.

#### 4. Results and discussion

Field emission from individual carbon nanotubes has been shown to exhibit Fowler–Nordheim emission behavior at low currents in the range of 0.4–80 nA [23]. However, previous reports have indicated that field emission can become unstable at currents above 0.1  $\mu\text{A}$  [24]. Fig. 5 shows a typical current–voltage profile obtained in these experiments and indicates that the emission current increases exponentially with increasing voltage as expected for field emission, although some irregularities are present at high values of the emission current. These irregularities are probably due to changes in the carbon nanotube emitter as the emission current increases. The inset in Fig. 5 displays the Fowler–Nordheim plot of the same data in which the quotient  $(I/V^2)$  are plotted as a function of  $1/V$  on a semi-logarithmic scale. The resulting curve is usually linear with a negative slope for metallic emitters. The change in slope that is evident in the inset data indicates a deviation from Fowler–Nordheim behavior, and is commonly observed for nanotube samples emitting over a large current range [9]. Each data point in Fig. 5 represents the mean of approximately 200 individual measurements taken at 0.308 s intervals at a constant voltage.

Measured field emission currents above 0.1  $\mu\text{A}$  regularly exhibited significant fluctuations when the applied voltage was increased or decreased. However, in many cases, the current remained reasonably stable up to values as high as 70  $\mu\text{A}$ , while the applied voltage was held constant. A typical current response as a function of time is shown in Fig. 6, in which a constant voltage of 446 V was maintained. The emission current was observed to fluctuate between 34 and 40  $\mu\text{A}$  for a period of time, and then at approximately 38 s, the current abruptly rose to a mean value of 47  $\mu\text{A}$ . This type of instability, where the emission

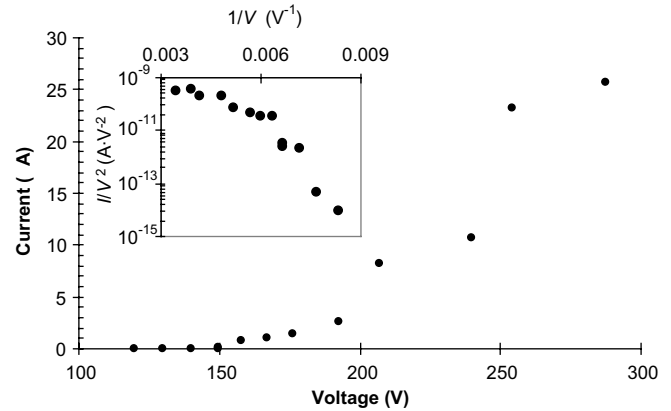


Fig. 5.  $I$ – $V$  characteristics for field emission from an individual MWNT. The vacuum gap is 2.6 mm.

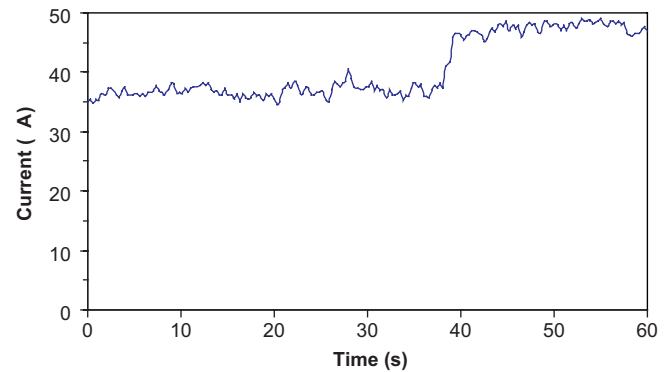


Fig. 6. Emission current plotted with time at an applied voltage of 446 V and an electrode gap of 2.6 mm.

current is reasonably stable over moderate time intervals, is typical of high-current field emission.

During the intervals in which the field emission remained reasonably stable, the anode temperature profile exhibited no noticeable temporal change and was characterized by taking the mean of five temperature data samples collected with an infrared camera at intervals of one second. For the experiment shown in Fig. 6, images were taken by the infrared camera during the time interval from 10 to 14 s. Fig. 7(a) shows the infrared image at 10 s. The anode temperature profile was measured along four lines extending radially from the point of maximum temperature on the anode surface, as shown in Fig. 7(a). Data lines 1a and 1b were aligned in the vertical direction, and data lines 2a and 2b were aligned in the horizontal direction. The total heating rate,  $Q$ , in Fig. 7(a) was determined to be approximately 16.4 mW by multiplying the applied voltage, 446 V, by the mean electric current measured in the interval 0–14 s shown in Fig. 6 approximately 36.7  $\mu\text{A}$ . The value calculated for the average electric current was found to depend on the time interval used in the calculation, causing an uncertainty in the average current of approximately 0.3  $\mu\text{A}$ . The uncertainty in the total heating was then found to be approximately 0.16 mW or 1%.

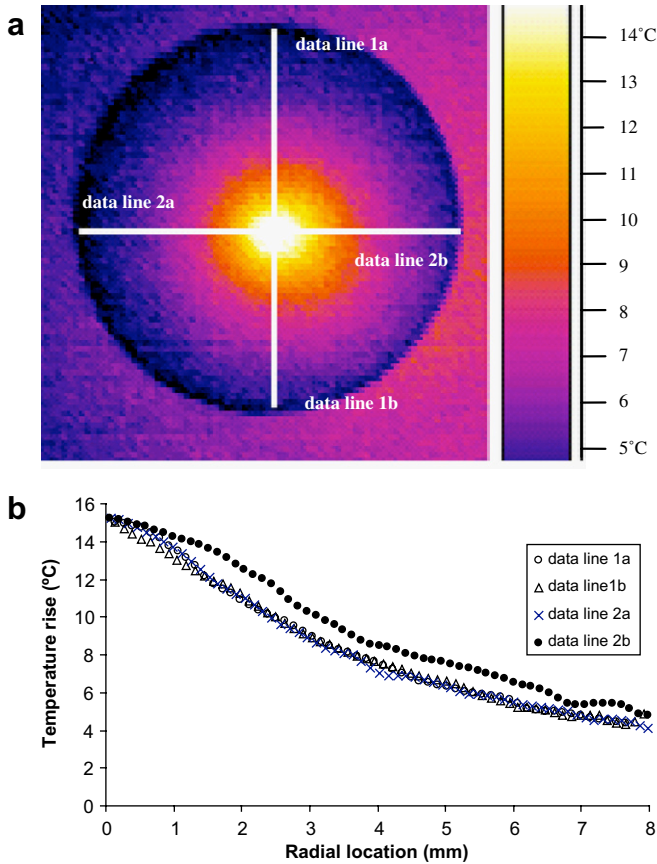


Fig. 7. (a) Infrared camera image of anode heating experiment. (b) Anode temperature rise obtained by averaging five data samples. The total heating on the anode surface was approximately 16.4 mW.

Fig. 7(b) displays the mean temperature profiles resulting from averaging the data taken by the infrared camera during the time interval 10–14 s in Fig. 6. The peak anode temperature rise, located approximately 1 mm directly below the geometric anode center, is 15.1 °C with an uncertainty of approximately  $\pm 0.4$  °C as calculated from Eq. (1). The mild asymmetry in the anode temperature profile observed in Fig. 7(b) indicates that the electron beam is slightly asymmetric with a greater density of electrons impacting the right side of the anode.

In the data presented in this study, the point of maximum temperature rise occurred within approximately 1 mm of the geometric anode center, thus ensuring that the observed asymmetry in the anode heating was due principally to asymmetry in the electron beam and not misalignment between the electron beam and the anode center. In additional experiments, however, the point of maximum temperature rise was observed to shift by as much as 3 mm as the applied voltage was adjusted. Also, in some cases, the location of peak temperature rise was seen to shift slowly in time before becoming stationary, indicating that the electron distribution in the beam depends on conditions at the nanotube tip in addition to the applied electric potential. Shifting of the location of

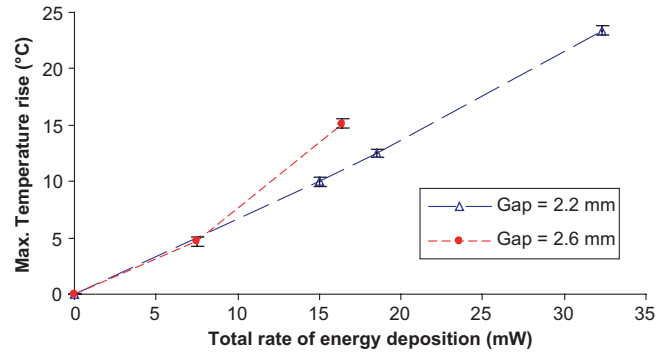


Fig. 8. Maximum anode temperature rises measured by an infrared camera in experiments with vacuum gaps of 2.2 and 2.6 mm, respectively.

the anode peak temperature rise due to field emission has also been reported by Harris et al. [7].

Similar experiments were conducted for different applied voltages, and maximum temperature rises of the anode are plotted as functions of the total heating rate in Fig. 8 for vacuum gaps of 2.2 and 2.6 mm. The error bars in Fig. 8 indicate the uncertainty in the temperature measurement. Table 1 summarizes the pertinent experimental results and includes the measurement uncertainties. As reported elsewhere [7], the peak temperature rise appears to increase nearly linearly with increased heating. Interestingly, however, the maximum temperatures for the experiment with the larger vacuum gap appear higher for similar heating values, indicating that conditions at the carbon nanotube emitter tip had a more significant effect on the size of the electron beam than did the vacuum gap separation. This result is consistent with electron trajectories in the vacuum gap determined by Monte Carlo simulations, which indicate that for the vacuum gaps listed in Table 1, the broadening of the electron beam is independent of the vacuum gap for the same level of power input. The approach utilized in the Monte Carlo simulations has been reported elsewhere [18].

As noted previously, the concentration of electrons in the beam was assumed to follow an axially symmetric Gaussian distribution, and the electron beam radius was characterized by the standard deviation,  $\sigma_e$ , which was determined by comparing the 1D finite-difference model results to the mean anode temperature profiles calculated

Table 1  
Experimental electron emission data from experiments with vacuum gaps of 2.2 and 2.6 mm, respectively

$V$ (V)	$I$ ( $\mu$ A)	$Q$ (mW)	$\Delta T$ (°C)
<i>Vacuum gap: 2.2 mm</i>			
349 $\pm$ 2	43.2 $\pm$ 0.3	15.0 $\pm$ 0.1	10.0 $\pm$ 0.4
351 $\pm$ 2	52.8 $\pm$ 0.3	18.5 $\pm$ 0.2	12.5 $\pm$ 0.4
405 $\pm$ 2	79.8 $\pm$ 0.5	32.3 $\pm$ 0.2	23.4 $\pm$ 0.4
<i>Vacuum gap: 2.6 mm</i>			
286 $\pm$ 2	26.1 $\pm$ 0.2	7.47 $\pm$ 0.08	4.7 $\pm$ 0.4
446 $\pm$ 2	36.7 $\pm$ 0.3	16.4 $\pm$ 0.2	15.1 $\pm$ 0.4

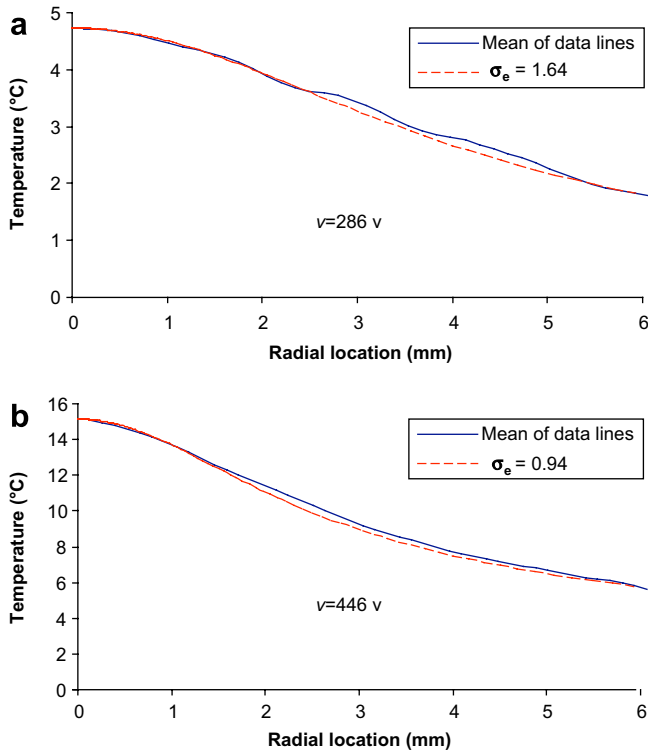


Fig. 9. Comparison of the mean anode temperature profiles with the temperature profiles predicted by the 1D finite-difference model. The applied voltages are 286 V (a) and 446 V (b), and the vacuum gap is 2.6 mm.

by averaging the four data lines recorded during each experiment. Fig. 9(a) and (b) shows the mean anode temperature profiles for the experiments in which the applied voltages were 286 and 446 V, respectively. Applying a least-squares fitting process, values of 1.64 and 0.94 mm were determined for  $\sigma_e$  under applied voltages of 286 and 446 V, indicating that the electron beam narrowed as the electric field increased. The anode temperature profiles predicted by the 1D finite-difference model using these values for  $\sigma_e$  are also plotted in Fig. 9, where a good fit is demonstrated between the data and the finite-difference model predictions.

In order to verify the results obtained from the 1D finite-difference model, a grid refinement study was performed, and the results were compared to those obtained from a 2D heat diffusion solver using commercial software. The results presented in Fig. 9 were obtained using 200 control volumes clustered more densely near the anode center and were determined to be grid independent to five decimal places. A similar grid refinement study performed for the 2D model showed that the results obtained from that model were grid-independent to three decimal places for 10 control volumes in the axial direction and 1000 control volumes in the radial direction. Although not shown in Fig. 9 for the purpose of clarity, the temperature profiles predicted by the 2D model almost exactly match those predicted by the 1D model for both applied voltages. The

maximum differences between the models occur at the peak temperatures and were less than 0.01 °C in Fig. 9(a) and less than 0.03 °C in Fig. 9(b). The close correspondence between the 1D and 2D models is expected because the temperature variation through the anode thickness is very small.

One additional comment is in order regarding Fig. 9. Contrary to what is usually expected from a least-squares fit, the model predictions in Fig. 9 are not equally balanced above and below the measured anode temperature profiles. The reason for this behavior is that the temperature in the outer region of the anode is determined almost exclusively by the temperature at the anode's outer edge. The distribution of electrons in the beam only affects the anode temperature profile inside the region directly impacted by the beam, and has negligible effect on the anode temperature profile outside this region. Because nearly the entire electron beam is concentrated on the anode surface within 4 mm from the point of maximum temperature, only data lying in this region affect the least-squares fit. Another consequence of this phenomenon is that weighting the least-squares fit more heavily near the anode center is unnecessary because the discrepancy between the temperature profiles given by the experimental data and the finite-difference model is naturally largest in the central portion of the anode. Consequently, for this study the least-squares error terms were equally weighted regardless of position on the anode surface.

In order to validate the conclusions drawn from the data, confidence intervals for the electron beam radius are necessary. The procedure that was followed to calculate the confidence intervals is demonstrated here by calculating the uncertainty associated with the data in Fig. 9(a). The uncertainty in the electron beam radius can be estimated from

$$u_{\sigma} = \sqrt{(u_{\sigma_{\text{fit}}})^2 + (u_{\sigma_T})^2 + (u_{\sigma_Q})^2 + (u_{\sigma_{\Delta z}})^2} \quad (5)$$

where  $u_{\sigma_{\text{fit}}}$ ,  $u_{\sigma_T}$ ,  $u_{\sigma_Q}$ , and  $u_{\sigma_{\Delta z}}$  are the respective uncertainties in the electron beam radius due to uncertainties in the least-squares fit, the infrared camera temperature measurement, the total heating on the anode surface, and the anode thickness. An estimate for the uncertainty in the electron beam radius associated with the least-squares fit may be obtained from

$$u_{\sigma_{\text{fit}}} = t_{95, N-1} S \sqrt{\frac{1}{\sum_{i=1}^N (\theta_{\sigma, i})^{-2}}} \quad (6)$$

where  $N$  is the number of data points used to determine the value of  $\sigma_e$ , and  $t_{95, N-1}$  is the  $t$  estimator corresponding to 95% probability and  $N - 1$  degrees of freedom.  $\theta_{\sigma, i}$  is the local sensitivity coefficient (the partial derivative of the predicted anode temperature rise with respect to  $\sigma_e$  at each data point  $i$ ) associated with  $\sigma_e$  in the least-squares fit. Lastly,  $S$  is an estimate of the variability of the data taken by the infrared camera and may be calculated using [21]

$$S = \sqrt{\frac{1}{N-1} \sum_{i=1}^N (T_{\text{data},i} - T_{\text{pred},i})^2} \quad (7)$$

where  $T_{\text{data},i}$  is the mean measured anode temperature rise at location  $r_i$ , and  $T_{\text{pred},i}$  is the predicted temperature rise at the same point.

Typically, approximately 45 measurements were taken along each data line to characterize the anode temperature profile. Employing Eq. (7), the variability in the data in Fig. 9(a) may be estimated as 0.08 °C as listed in Table 2. This estimate of the variability is inflated by the relative poorness of the model fit at intermediate radial locations; however, it does provide an upper limit to the variability and hence is useful in approximating the uncertainty in the electron beam radius due to the least-squares fit. Setting the  $t$  estimator equal to 2.021 [21], the uncertainty in the beam radius due to the least-squares fit is estimated from Eq. (6) as 0.04 mm.

The uncertainty in the electron beam radius due to the infrared camera temperature measurement,  $u_{\sigma T}$ , may be estimated by dividing the uncertainty in the anode peak temperature rise as given in Table 1 by the local sensitivity coefficient,  $\theta_{\sigma,r=0}$ , at  $r=0$ . Approximate values for all of the sensitivity coefficients were obtained using the 1D finite-difference model as described by Figliola [25], and in this process a value of 1.5 °C/mm as found for  $\theta_{\sigma,r=0}$ , yielding a value of approximately 0.26 mm for  $u_{\sigma T}$  as given in Table 2.

The uncertainty in the beam radius due to the total heating uncertainty,  $u_{\sigma Q}$ , may be estimated from

$$u_{\sigma Q} = u_Q \frac{\theta_{Q,r=0}}{\theta_{\sigma,r=0}} \quad (8)$$

where  $u_Q$  is the uncertainty in the total anode heating as given in Table 1 and  $\theta_{Q,r=0}$  is the sensitivity coefficient corresponding to the partial derivative at  $r=0$  of the predicted temperature rise with respect to total heating. A value of 0.23 °C/mW was found for  $\theta_{Q,r=0}$ , giving an estimate of 0.03 mm for  $u_{\sigma Q}$ .

The uncertainty in the beam radius due to the anode thickness uncertainty,  $u_{\sigma \Delta z}$ , may be estimated from

$$u_{\sigma \Delta z} = u_{\Delta z} \frac{\theta_{\Delta z,r=0}}{\theta_{\sigma,r=0}} \quad (9)$$

where  $u_{\Delta z}$  is the uncertainty in the anode thickness, taken as 0.0013 mm, and  $\theta_{\Delta z,r=0}$  is the sensitivity coefficient corre-

Table 2  
Estimated uncertainty parameters involved in calculating the 95% confidence interval for electron beam radius in Fig. 9(a)

$S$ (°C)	0.08
$u_{\sigma \text{fit}}$ (mm)	0.04
$u_{\sigma T}$ (mm)	0.26
$u_{\sigma Q}$ (mm)	0.03
$u_{\sigma \Delta z}$ (mm)	0.05
$u_{\sigma}$ (mm)	0.27

sponding to the partial derivative at  $r=0$  of the model temperature rise with respect to anode thickness. The value of  $\theta_{\Delta z,r=0}$  found from the 1D finite-difference model is 56.9 °C/mm, yielding a value of 0.05 mm for  $u_{\sigma \Delta z}$ . Substituting the values of  $u_{\sigma \text{fit}}$ ,  $u_{\sigma T}$ ,  $u_{\sigma Q}$ , and  $u_{\sigma \Delta z}$  from Table 2 into Eq. (5), the total uncertainty in the electron beam radius in Fig. 9(a) is estimated as 0.27 mm. Comparing the uncertainty terms in Table 2, it is found that the uncertainty associated with temperature measurement dominates the overall uncertainty in the electron beam radius, and the same trend is seen for all the measurements.

Fig. 10 displays the relationship between the electron beam radius and the emission current for all the experiments listed in Table 1 and indicates that the beam radius decreases as the emission current or applied voltage increases. The error bars represent the uncertainties in electron beam radius calculated for each point using the procedure outlined above. The first two data points for the experiments having a vacuum gap of 2.2 mm are of particular interest because of the overlap in their confidence intervals. As shown in Table 1, the applied voltages for these experiments are nearly equal; thus, the overlap in the confidence intervals of the electron beam radii is not surprising.

A key element in assessing anode performance is the maximum heat flux on the anode surface produced by the electron beam. An estimate of the maximum heat flux,  $q''_{\text{max}}$ , in each experiment may be obtained by substituting into Eq. (3) the respective values of the electron beam radius and total heating. The estimated maximum heat fluxes are listed along with the electron beam radii in Table 3. The uncertainties in  $q''_{\text{max}}$  listed in Table 3 were calculated using [25]

$$u_{q''_{\text{max}}} = \sqrt{(u_Q \phi_Q)^2 + (u_{\sigma} \phi_{\sigma})^2} \quad (10)$$

where  $u_{\sigma}$  is the uncertainty in the electron beam radius given in Table 3.  $\phi_Q$  and  $\phi_{\sigma}$  are the sensitivity coefficients corresponding to the partial derivatives of  $q''$  at  $r=0$  with respect to  $Q$  and  $\sigma_e$ , respectively. We note that the uncer-

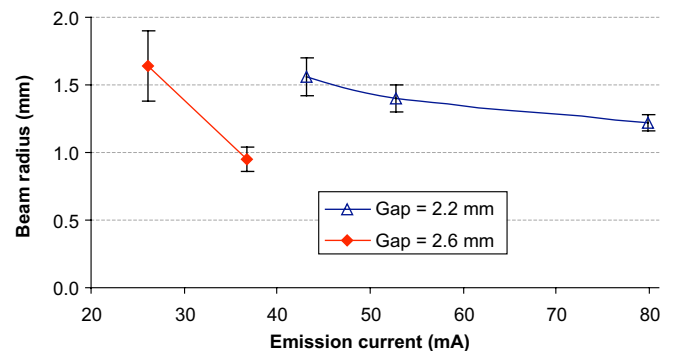


Fig. 10. Predicted electron beam radius versus emission current for the experiments listed in Table 1.

Table 3  
Summary of observations for experiments with vacuum gaps of 2.2 and 2.6 mm

$V$ (V)	$Q$ (mW)	$\sigma_e$ (mm)	$q''_{\max}$ (W/cm <sup>2</sup> )
<i>Vacuum gap: 2.2 mm</i>			
349 ± 2	15.0 ± 0.1	1.56 ± 0.14	0.1 ± 0.0012
351 ± 2	18.5 ± 0.2	1.40 ± 0.10	0.15 ± 0.0017
405 ± 2	32.3 ± 0.2	1.22 ± 0.06	0.35 ± 0.0036
<i>Vacuum gap: 2.6 mm</i>			
286 ± 2	7.47 ± 0.08	1.64 ± 0.26	0.044 ± 0.0006
446 ± 2	16.4 ± 0.2	0.94 ± 0.09	0.295 ± 0.004

tainties in Fig. 10 and Table 3 assume the electron beam is perfectly symmetric and must be regarded simply as first-order approximations.

Plotting the heat flux profiles predicted by the finite-difference model illustrates electron beam narrowing at high electric fields because the electron flux at a given location on the anode surface is proportional to the heat flux at that point. Heat flux profiles for the experiments in which the applied voltages were 286 and 446 V are shown on a logarithmic scale in Fig. 11. The heat flux profile (or electron flux profile) associated with the higher potential is clearly narrower and actually exhibits a lower flux for radial locations exceeding 2.5 mm from the point of peak temperature rise.

The data in Table 3 also indicate that the relationship between  $Q$  and  $q''_{\max}$  is nonlinear. For the experiment in which the vacuum gap was 2.6 mm, as the applied voltage increased from 286 V to 446 V,  $Q$  increased by a factor of 2.2 while  $q''_{\max}$  increased by a factor 6.8. If  $\sigma_e$  were constant, then  $Q$  would be proportional to  $q''_{\max}$  for all experiments; however, because the electron beam narrows as the applied voltage increases,  $q''_{\max}$  grows much faster than  $Q$ . This phenomenon becomes particularly important when considering anode performance at high rates of energy deposition. The resulting local heat fluxes on the anode surface can lead to significant local temperature rises in the anode and possibly anode failure.

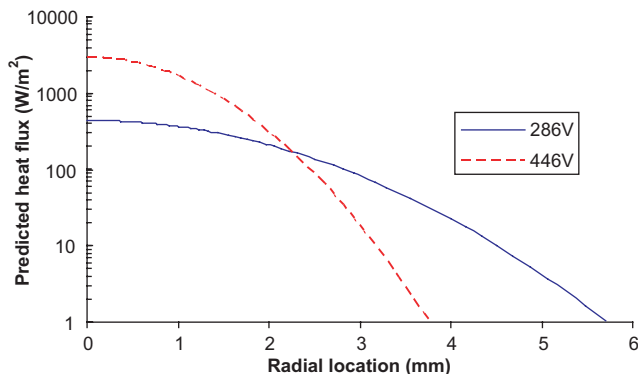


Fig. 11. Predicted heat fluxes based on 1D finite-difference model for the experiments in which the applied voltages were 286 and 446 V. The total heating on the anode surface was 7.47 and 16.4 mW, respectively.

## 5. Conclusion

Significant anode heating resulting from electron field emission in vacuum has been observed. Experiments indicate the thermal energy deposition distribution can be approximated by a Gaussian profile, and the electron beam radius becomes narrower as the electrical potential increases and depends on emission conditions at the emitter tip. The narrowing of the electron beam radius may be at least partially explained by observing that higher electric potentials accelerate the electrons more rapidly toward the anode, thereby decreasing the electron transit time and reducing the spread of the electron beam at the anode surface.

Several approximations were made to estimate the value of  $\sigma_e$  for the experiments in this study. As indicated by the data in Fig. 7(b), the electron beam is not perfectly symmetric. This effect was neglected in the present work but could be included in future work to obtain more accurate models of the actual electron beam distribution. Another factor not investigated in this work involves shifting of the location of the anode peak temperature with time observed in some experiments at a constant applied electric potential. This phenomenon indicates that the electron beam is affected by emission conditions at the emitter tip. Future experiments could study a possible correlation between total emission current and shifts in position of the electron beam over time.

## Acknowledgments

The authors wish to thank numerous colleagues for their assistance in this research. From the Nanoscale Thermo-Fluids Laboratory at Purdue University, Matt Maschmann and Sungwon Kim provided the nanotube samples, and Mike Peterson and Jun Xu assisted in mounting the nanotubes on the etched tungsten tips. The authors also appreciate Dr. Ronald G. Reifenberger and the Nanoscale Physics Laboratory (Purdue University) for the use of equipment in their laboratory, including the Nikon Epiphot 200 microscope.

We wish to acknowledge the use of Fluent Inc.'s solver FLUENT/UNS and its mesh generator GAMBIT in this work. We also gratefully acknowledge funding by the National Science Foundation through the NIRT and CAREER programs.

## References

- [1] I. Brodie, P.R. Schwoebel, Vacuum microelectronic devices, Proc. IEEE 82 (1994) 1006–1018.
- [2] J.A. Nation, L. Schachter, F.M. Mako, L.K. Len, W. Peter, C.M. Tang, T. Srinivasan-Rao, Advances in cold cathode physics and technology, Proc. IEEE 87 (1999) 865–889.
- [3] J.M. Bonard, J.P. Salvetat, T. Stöckli, W.A. de Heer, L. Forro, A. Chätelain, Field emission from single-wall carbon nanotube films, Appl. Phys. Lett. 73 (7) (1998) 918–920.
- [4] W.P. Kang, T.S. Fisher, J.L. Davidson, Diamond microemitters – the new frontier of electron field emissions and beyond, New Diamond Frontier Carbon Technol. 11 (2) (2001) 129–146.

- [5] P. Grant, C. Py, C. Mößner, A. Blais, H. Tran, M. Gao, Electron field emission from diamond-like carbon, a correlation with surface modifications, *J. Appl. Phys.* 87 (3) (2000) 1356–1360.
- [6] T.S. Fisher, D.G. Walker, R.A. Weller, Analysis and simulation of anode heating from electron field emission, *IEEE Trans. Compon. Pack. Technol.* 26 (2) (2003) 317–323.
- [7] C.T. Harris, D.G. Walker, T.S. Fisher, W.H. Hofmeister, Experimental characterization of anode heating due to electron field emission, *Microscale Thermophys. Eng.* 8 (2) (2004) 101–109.
- [8] R.H. Fowler, L.W. Nordheim, Field emission from metallic surfaces, *Proc. Royal Soc. Lond. A* 119 (1928) 173–181.
- [9] C.A. Spindt, A thin film field emission cathode, *J. Appl. Phys.* 39 (1968) 3504–3505.
- [10] J.M. Bonard, H. Kind, T. Stöckli, L.O. Nilsson, Field emission from carbon nanotubes: the first five years, *Solid-State Electron.* 45 (6) (2001) 893–914.
- [11] S.B. Sinnott, R. Andrews, Carbon nanotubes: synthesis, properties, and applications, *Crit. Rev. Solid State Mater. Sci.* 26 (3) (2001) 145–249.
- [12] M.S. Dresselhaus, Burn and interrogate, *Science* 292 (5517) (2001) 650–651.
- [13] W. Zhu, C. Bower, O. Zhou, G. Kochanski, S. Jin, Large current density from carbon nanotube field emitters, *Appl. Phys. Lett.* 75 (6) (1999) 873–875.
- [14] Y. Saito, K. Hamaguchi, K. Hata, K. Uchida, Y. Tasaka, F. Ikazaki, M. Yumura, A. Kasuya, Y. Nishina, Conical beams from open-ended nanotubes, *Nature* 389 (1997) 554–555.
- [15] A. Mayer, N.M. Miskovsky, P.H. Cutler, Photon-stimulated field emission from semiconducting (10,0) and metallic (5,5) carbon nanotubes, *Phys. Rev. B* 65 (19541) (2002) 1–6.
- [16] A. Mayer, N.M. Miskovsky, P.H. Cutler, Simulations of field emission from a semiconducting (10,0) carbon nanotube, *J. Vac. Sci. Technol. B* 20 (2002) 100–104.
- [17] A. Mayer, N.M. Miskovsky, P.H. Cutler, Transfer-matrix simulations of field emission from a metallic (5,5) carbon nanotube, *Ultramicroscopy* 92 (2002) 215–220.
- [18] D.G. Walker, T.S. Fisher, W. Zhang, Simulation of field-emitted electron trajectories and transport from carbon nanotubes, *J. Vac. Sci. Technol. B* 22 (3) (2004) 1101–1107.
- [19] J.P. Ibe, P.P. Bey Jr., S.L. Brandow, R.A. Brizzolara, N.A. Burnham, D.P. DiLella, K.P. Lee, C.R.K. Marrian, R.J. Colton, On the electrochemical etching of tips for scanning tunneling microscopy, *J. Vac. Sci. Technol. A* 8 (4) (1990) 3570–3575.
- [20] R. Andrews, D. Jacques, A.M. Rao, F. Derbyshire, D. Qian, X. Fan, E.C. Dickey, J. Chen, Continuous production of aligned carbon nanotubes: a step closer to commercial realization, *Chem. Phys. Lett.* 303 (1999) 467–474.
- [21] A.H. Bowker, G.J. Lieberman, *Engineering Statistics*, second ed., Prentice Hall, New Jersey, 1972, pp. 346–349, 603.
- [22] B.M. Guenin, Conduction heat transfer in a printed circuit board, *Electron. Cooling Mag.* 4 (2) (1998).
- [23] J.M. Bonard, F. Maier, T. Stockli, A. Châtelain, W.A. de Heer, J.P. Salvetat, L. Forro, Field emission properties of multiwalled carbon nanotubes, *Ultramicroscopy* 73 (7) (1998) 7–15.
- [24] N. de Jonge, N.J. van Druten, Field emission from individual multiwalled carbon nanotubes prepared in an electron microscope, *Ultramicroscopy* 95 (2003) 86–91.
- [25] R.S. Figliola, D.E. Beasley, *Theory and Design for Mechanical Measurements*, third ed., Wiley, New York, 2000, p. 161.